Research Article

Xiaowei Zhu, Yue Li, Yilun Shi, Lanjie Hou, Guoxian Wang, Zhoukun He*, and Xiaorong Lan*

Structure–mechanical property relationships of 3D-printed porous polydimethylsiloxane films

https://doi.org/10.1515/ntrev-2023-0188
received June 27, 2023; accepted December 21, 2023

Abstract: Complex microstructures can be produced from different base materials by combining three-dimensional (3D) printing technology and ink formulations. The surface wettability of the 3D-printed porous polydimethylsiloxane (PDMS), particularly its superhydrophobic property, strongly depends on its physical structure. However, the mechanism underlying the effect of the microporous structure on the mechanical properties is not understood, which seriously constrains the structural–functional integration design of the 3D-printed superhydrophobic porous PDMS. To solve this problem, we studied the influence of the printing parameters on the mechanical properties in the compression and tension directions using a finite element method. The results showed that the load transfer path of the 3D-printed porous PDMS was along the overlapping area of the adjacent filaments. As the filament spacing decreased or the filament diameter increased, the elastic modulus of the porous PDMS was enhanced, improving its resistance to tensile and compressive deformation. A quantitative relationship was established between the relative densities of the porous PDMS films and their relative elastic moduli.

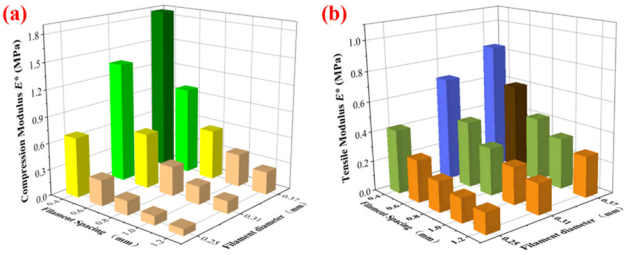

Graphical abstract

This study presents a numerical simulation of the structure–mechanical relationship of 3D-printed porous polydimethylsiloxane (PDMS) films with superhydrophobic properties. The influence of the printing parameters (filament spacing and filament diameter) on the mechanical properties was studied in the compression and tension directions using a finite element method. The results showed that the load transfer path of the 3D-printed porous PDMS was along the overlapping area of the adjacent filaments. As the filament spacing decreased or the filament diameter increased, the elastic modulus of the porous PDMS was enhanced, improving its resistance to tensile and compressive deformation.

This study provides theoretical guidance for the structural–functional integration design of 3D-printed superhydrophobic porous PDMS.

Keywords: PDMS, 3D printing, mechanical properties

*** Corresponding author: Zhoukun He,** Institute for Advanced Study, Research Center of Composites & Surface and Interface Engineering, Chengdu University, Chengdu, 610106, China, e-mail: hezhoukunhe@163.com
*** Corresponding author: Xiaorong Lan,** Luzhou Key Laboratory of Oral & Maxillofacial Reconstruction and Regeneration, The Affiliated Stomatological Hospital, Southwest Medical University, Luzhou, 646000, China; Basic Medicine Research Innovation Center for Cardiometabolic Diseases, Ministry of Education, Southwest Medical University, Luzhou, 646000, China; Institute of Stomatology, Southwest Medical University, Luzhou, 646000, China, e-mail: xiaoronglancdm@163.com
Xiaowei Zhu: Henan Key Laboratory of Grain and Oil Storage Facility & Safety, Henan University of Technology, Zhengzhou, 450001, China; School of Civil Engineering, Henan University of Technology, Zhengzhou, 450001, China
Yue Li, **Yilun Shi**, **Lanjie Hou:** School of Civil Engineering, Henan University of Technology, Zhengzhou, 450001, China
Guoxian Wang: Department of Innovative Materials Renewable Design, Kookmin University, Seoul, 02707, Republic of Korea

1 Introduction

After billions of years of selection, some plants and animals have evolved functional surfaces with specific wettabilities [1–12], including superhydrophobicity and anisotropic surface wettability (ASW), showing a wide range of important applications in self-cleaning surfaces [13–15], antifouling [16–21], directional water or fog collection or transportation [22–25], *etc.* [26–31]. For example, the combination of micro- and nanoscale papillae and low surface energy waxes makes lotus leaves superhydrophobic with a water contact angle (WCA) greater than 150°, resulting in strong water repellency. For the ASW surfaces, such as rice leaves and butterfly wings [32–34], the static WCAs and dynamic

water rolling angles vary in different directions, allowing water droplets to move in only one direction. This special surface wettability is usually attributed to the physical discontinuity and chemical heterogeneity of the biological surfaces, inspiring considerable research interest from both the scientific and industrial communities [35,36].

In recent decades, it has been recognized that the specific surface wettability of biological surfaces is largely dependent on their unique micro- and nanostructures and surface chemistry. Various methods have been developed to create biomimetic surfaces with specific surface wettabilities [37–40]. For example, dip coating [41], spray coating [42], and chemical or physical etching [43] have been used to create micro- and nanoscale roughness with low surface energies. These methods usually involve multistep processing with limited precision in structural control, resulting in random surface structures, defects, and poor durability on the prepared superhydrophobic surfaces. Moreover, to achieve ASW, additional modulation of the chemical composition or physical structure at the micro- and nanoscales is often required [44,45], which involves complex manufacturing processes and expensive equipment. For example, laser etching has been used to create asymmetric geometric (topographic) structures (*e.g.*, grooves and fibers) and anisotropic wetting surfaces [46,47].

In recent years, 3D printing technologies have attracted increasing attention in constructing specific surfaces and micro- and nanostructures owing to the advantages of flexible design and manufacturing freedom [48–54]. For direct ink writing (DIW) 3D printing, structural control can be achieved by modulating the ink formulation and printing parameters. In our previous study, the physical structure and surface wettability of the polydimethylsiloxane (PDMS) film were controlled by regulating the printing parameters (*e.g.*, filament spacing and filament diameter) to produce porous PDMS with superhydrophobic properties and good mechanical stability [2,13]. In addition, the structures of the regular porous PDMS or other thermoplastic elastomers containing hydrophobic silica or other types of nanoparticles were further optimized for various applications [55–57]. Adjusting the porous structure of the 3D-printed PDMS not only modulates its superhydrophobic properties but also has a significant impact on its mechanical properties [58–61].

However, there is a lack of theoretical guidance to correlate the structural parameters with the mechanical properties of the porous PDMS with superhydrophobic performance. Therefore, based on previous experiments, this study presents a quantitative analysis of the influence of structural parameters (filament diameter and filament spacing) on the mechanical properties (compression and tension strengths) of the 3D-printed superhydrophobic porous PDMS using an FEM. This study provides theoretical guidance on the structural design for the preparation of mechanically stable superhydrophobic regularized porous PDMS *via* 3D printing. The established relationships between structure and mechanical property are also useful for the structure–function integration in designing adaptive robotics, biomaterials, waterproof protection, and directional transport.

2 Methods

2.1 Preparation of 3D-printed porous PDMS

Based on the pre-planned printing path (Figure 1a) [2], the PDMS printing ink (Dow Corning SE1700) was extruded from the nozzle with a typical 150 μm inner diameter in the form of filaments by DIW 3D printing technology. The PDMS printing ink was printed layer by layer to form four-layer porous structural features (Figure 1b). The default 3D printing parameters to design porous PDMS film are

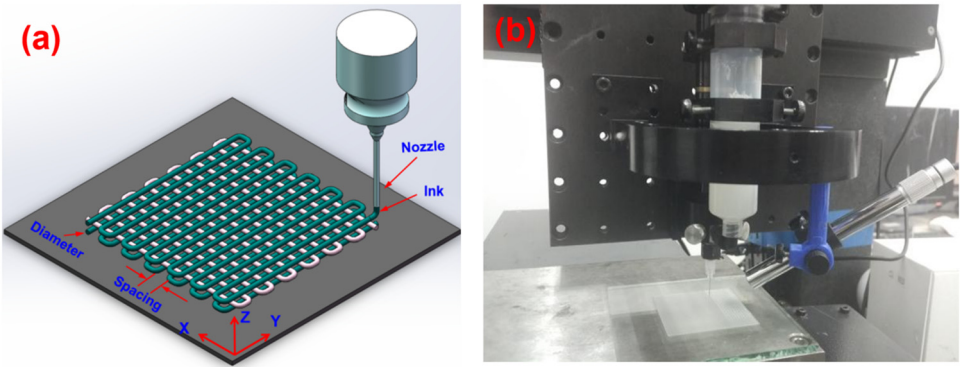

Figure 1: (a) Scheme and (b) snapshot of the 3D printing process of porous PDMS films.

Table 1: FEM simulation conditions for porous PDMS

Model number	Print layers	Filament diameter d (mm)	Filament spacing/(mm)	Porosity φ (%)
Foam-4-0.37-0.4	4	0.37	0.4	10.1
Foam-4-0.37-0.6			0.6	34.4
Foam-4-0.37-0.8			0.8	48.5
Foam-4-0.37-1.0			1.0	57.8
Foam-4-0.37-1.2			1.2	64.3
Foam-4-0.31-0.4	4	0.31	0.4	24.2
Foam-4-0.31-0.6			0.6	47.2
Foam-4-0.31-0.8			0.8	59.5
Foam-4-0.31-1.0			1.0	67.3
Foam-4-0.31-1.2			1.2	72.4
Foam-4-0.25-0.4	4	0.25	0.4	42.3
Foam-4-0.25-0.6			0.6	61.1
Foam-4-0.25-0.8			0.8	70.7
Foam-4-0.25-1.0			1.0	76.5
Foam-4-0.25-1.2			1.2	80.3

summarized in Table 1. Then, the 3D-printed porous PDMS was transferred to an oven and cured at 125°C for 24 h. The structural characteristics of the porous PDMS determine its hydrophobicity and mechanical properties. To analyze the deformation mechanism and internal stress state of the porous PDMS under uniaxial loading, the influence of the printing parameters on the mechanical properties was studied in the compression and tension directions using an FEM.

2.2 Constitutive model for PDMS

In this study, the mechanical properties of the PDMS matrix materials were characterized based on the Mooney–Rivlin model [62], as shown in equation (1):

$$U = C_{10}(I_1 - 3) + C_{01}(I_2 - 3) + \frac{1}{D_1}(J - 1)^2, \quad (1)$$

where U is the strain energy of the materials; C_{10} and C_{01} are the fitted material coefficients, respectively; I_1 and I_2 are the first and second invariants of the strain bias, respectively; J is the elastic volume ratio; and D_1 determines the compressibility of the material.

The fitting of the parameters of the superelastic constitutive model for rubber materials needs to be based on uniaxial tensile and compression tests, biaxial tensile and compression tests, planar tensile and compression tests, and volumetric tensile and compression tests. The more data from the aforementioned tests, the more accurate the model, but considering the cost of the tests, the uniaxial experimental data are often fitted to obtain the parameters of the superelastic constitutive model and the stability of the model in terms of other mechanical behaviors is evaluated based on the finite element analysis program. Because the intrinsic model we obtained was evaluated to have better stability in other mechanical properties, its complex mechanical behavior characteristics can be better restored. Thus, the material properties of PDMS obtained based on the compression test are suitable to be used for the tensile test sample. Therefore, in this study, only the uniaxial compressive behavior of the PDMS block was tested using a universal material testing machine (CTM4304S, Shenzhen Suns Technology Stock Co., LTD, China) at a loading rate of 2 mm/s based on the international standard (ISO 7743-2017). Owing to the stress-softening phenomenon of the PDMS material, the third loading test dataset was selected to characterize its uniaxial compression performance.

Based on the constitutive model, the measured compressive stress–strain data of the PDMS block were fitted using the corresponding parameters (C_{10}, C_{01}, and D_1), and their final fitted values were 0.203741993, 0.08319049733, and 0.177210526, respectively. Numerical simulations of the PDMS block compression were first performed (Figure 2), and the experimental results were in good agreement with the simulated data, implying that the model could reflect the mechanical characteristics of the PDMS.

2.3 FEM

Considering that the 3D-printed porous PDMS had a regular structure in the scanning electron microscopy (SEM) image, an FEM was constructed to reflect the structural characteristics shown in the SEM image (Figure 3a). The *x-y* plane was the in-plane orientation of the porous PDMS model (Figure 3b), and the layers of the PDMS filaments,

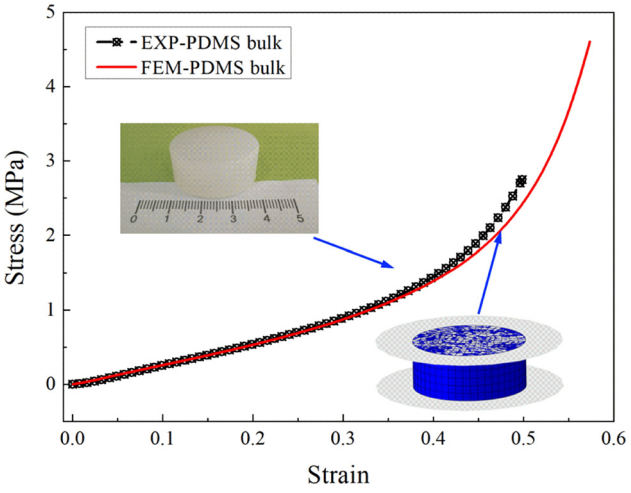

Figure 2: Comparison between experimental and numerical simulation of the compression behaviors of PDMS bulk.

except for the first layer, were cylindrical with six filaments per layer. The *z*-direction represented the height of the four layers of porous PDMS. The layer height (*h*, the distance between the center of the filament of adjacent layers) was 0.2 mm. The filaments in the intervening layer were aligned (Figure 3c). Boolean operation was used to remove the overlapping area of the upper and lower layers, and the entire porous PDMS model was considered. The SEM image and FEM of the porous PDMS with a filament diameter (*d*) of 0.37 mm and a filament spacing (*l*) of 0.6 mm were compared, and their structural characteristics were relatively consistent (Figure 3d and e) [2]. However, because the filament diameter (*d*, 0.37 mm) was close to two times the layer height (*h*, 0.2 mm) of the neighboring print layer, there might be sinking due to the overweight of the PDMS filament, which produced the phenomenon that the spacer layers were connected to the PDMS filament (Figure 3e). Although the actual 3D-printed PDMS films were hardly impossible to match the idealized FEM, the idealized FEM could show the force transfer path and deformation mechanism under compressive and tensile loads more clearly, and these conclusions could provide a reference to understand the force transfer path and deformation mechanism of actual 3D-printed PDMS films.

2.4 Working condition design

To study the influence of structural parameters on the mechanical properties (compression and tension) of 3D-printed superhydrophobic porous PDMS, a finite element simulation model was designed with the filament diameter and spacing as variables. The filament diameters (*d*) varied from 0.37, 0.31, to 0.25 mm by changing the printing speed from 0.75, 1.00, to 2.00 mm/s, while the spacing of the adjacent filaments was increased from 0.4, 0.6, 0.8, 1.0, to 1.2 mm. These variables were combined orthogonally to design a geometric model. The layer height (*h*) was fixed as 0.2 mm. The operating conditions are listed in Table 1. Based on the geometry of the 3D-printed porous PDMS

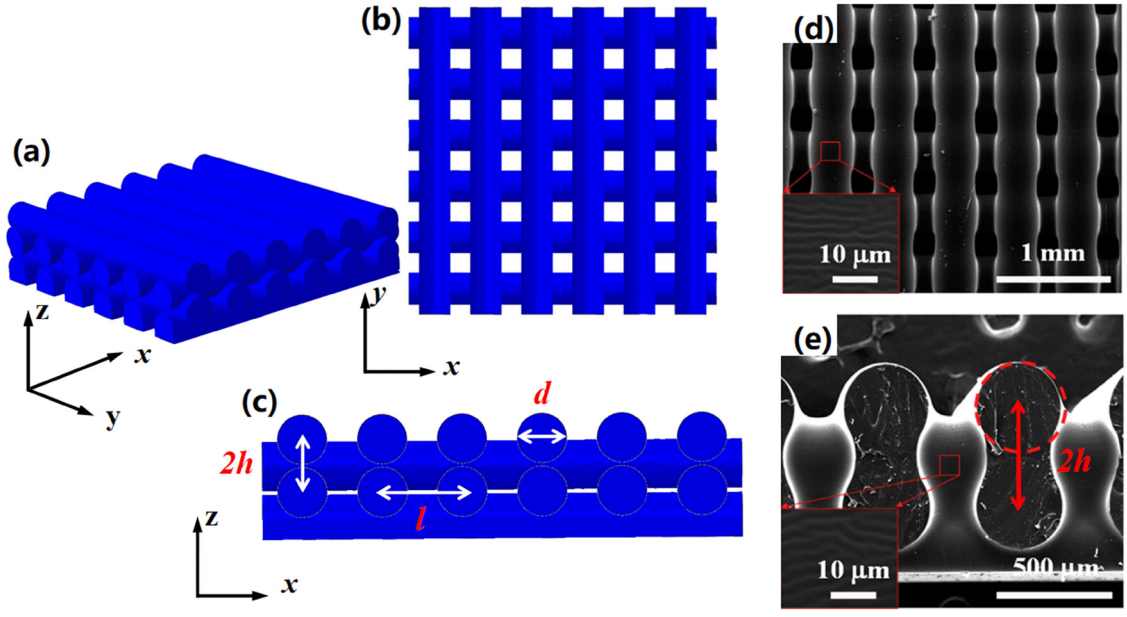

Figure 3: Comparison of physical structure of 3D-printed porous PDMS: (a) a whole FEM, (b) top-layer, and (c) cross-sectional physical features of an FEM, and (d and e) SEM images of the 3D-printed porous PDMS at different magnifications. Reprinted with permission from Ref. [2], Copyright 2017, Elsevier Ltd.

films, the foam porosity (φ) was extracted from the finite element analysis program.

3 Results and discussion

3.1 Influence of structural parameters on the compression properties of porous PDMS

The hyperelastic behavior of 3D-printed porous PDMS films under compressive loading was similar to that of traditional foam materials. As shown in Figure 4a, the compressive stress of the porous PDMS increased linearly with the compressive strain until the strain reached 10%. To explore the deformation mechanism of the porous

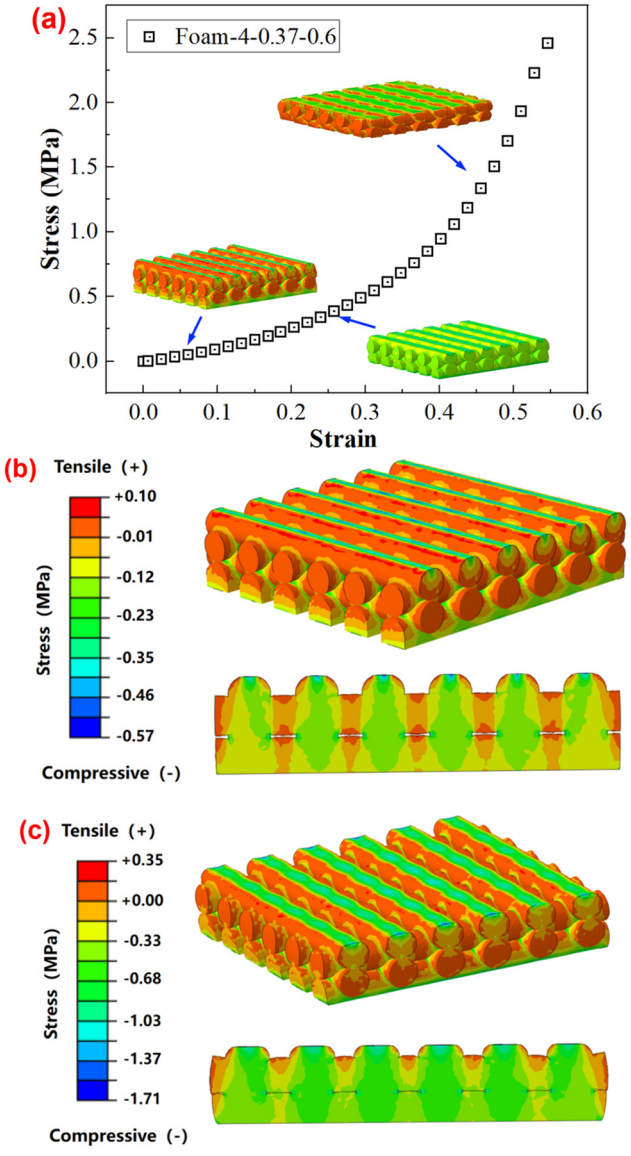

Figure 4: Compression behaviors of porous PDMS model: (a) compressive stress–strain curve. Stress distributing graph in the *x*-*z* section of the model "Foam-4-0.37-0.6" at (b) 5% compressive strain and (c) 20% compressive strain.

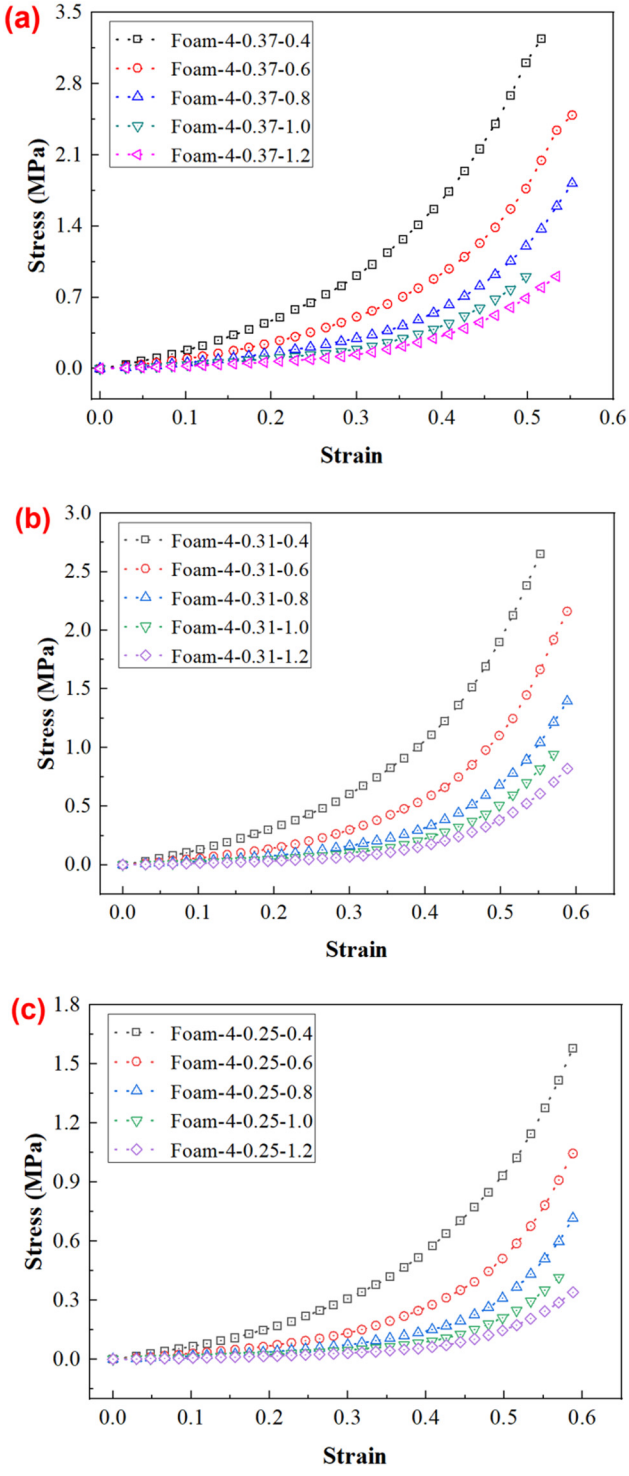

Figure 5: Effect of filament spacing on the compressive behaviors of 3D-printed porous PDMS films with different filament diameters: (a) 0.37 mm, (b) 0.31 mm, and (c) 0.25 mm.

PDMS film at this stage, the stress cloud of the *x*-*z* section was obtained for "Foam-4-0.37-0.6" (Figure 4b). The compressive stresses in the *z*-direction of the 3D-printed PDMS were mainly transferred in a columnar pattern (yellow or green area in Figure 4b) from the top to the bottom along the overlapping area of adjacent layers. The stress values in the overlapping region were significantly higher than those in the non-overlapping region for the porous PDMS model. Thus, the compressive modulus of the elasticity of the porous PDMS films was mainly attributed to the axial deformation mechanism of these columns. As the compressive strain increased to 20%, the internal pores of the porous PDMS film gradually collapsed, and the stress distribution was homogenized, accelerating the stress growth (Figure 4c). At 40% compressive strain, the stress column in the porous films completely disappeared, and this densification state resulted in a rapid increase in the compressive stress.

Figure 5 shows the effect of filament spacing on the compression behavior of the porous PDMS with filament diameters of 0.37, 0.31, and 0.25 mm. When the filament diameter (*d*) was fixed, the resistance to compression deformation gradually increased as the filament spacing (*l*) decreased. At a specific filament spacing, the resistance to compressive deformation was gradually enhanced with the increase in the filament diameter (*d*). A larger filament diameter or a smaller filament spacing could decrease the porosity and increase the relative density of the porous PDMS, which is the main reason for the enhancement in its resistance to compressive deformation.

Therefore, by adjusting the diameter and spacing of the filaments, the compressive behavior could be regulated. As shown in Figure 6a, the compressive modulus E^* in all FEMs reached a minimum of 0.07 MPa and a maximum of 1.83 MPa. To analyze the modulation mechanism quantitatively, the aforementioned data were fitted based on the relationship between the relative elastic modulus and the relative density of conventional foam materials (equations (2) and (3)) [63]:

$$\frac{\rho^*}{\rho_S} = \frac{\pi d^2}{4hl}, \tag{2}$$

$$\frac{E^*}{E_S} = C\left(\frac{\rho^*}{\rho_S}\right)^n, \tag{3}$$

where ρ^* and ρ_S are the density of the porous and solid PDMS film, and C and n are the fitting coefficients, and E_S is the elastic modulus of solid PDMS, which is approximately 2.58 MPa.

As shown in Figure 6b, the predicted curves are in good agreement with the simulated data, suggesting that the FEMs can provide theoretical guidance for the design of 3D-printed PDMS with superhydrophobic properties in terms of compressive mechanical behavior.

3.2 Influence of structural parameters on the tensile properties of porous PDMS

The uniaxial tensile behavior of 3D-printed porous PDMS films was similar to that of traditional rubber materials.

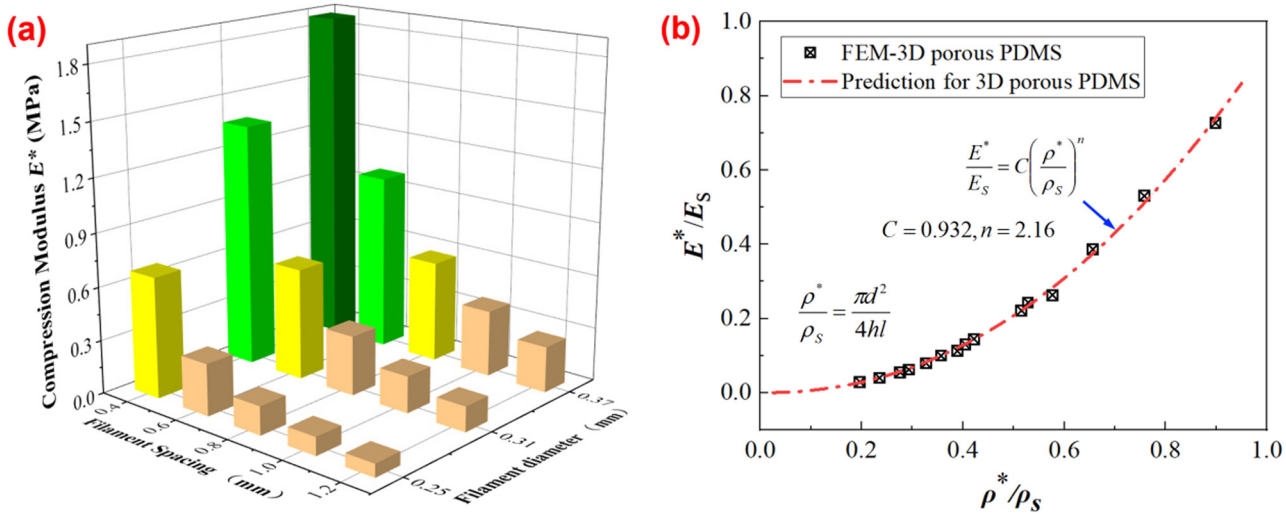

Figure 6: (a) Effects of the filament diameter and filament spacing on the compressive elastic modulus E^*. The histograms within the same color represent similar compressive elastic modulus E^*, and (b) relationship between the relative elastic modulus and the relative density of 3D-printed porous PDMS.

Initially, the tensile stress increased linearly with increasing strain until the strain reached 15% (Figure 7a). To visualize the deformation mechanism of the porous PDMS, the Von-Mises stress cloud was obtained for model "Foam-4-0.37-0.6" at 100% tensile strain (Figure 7b). The internal stresses of the 3D-printed PDMS mainly transferred along the filaments parallel to the direction of the tensile force (green area in Figure 7b). The stress values in this region were significantly higher than those in the filament (blue area in Figure 7b) perpendicular to the direction of the tensile force. Thus, the 3D-printed porous PDMS is a typical orthotropic material, and its linear tensile modulus is mainly attributed to the filaments parallel to the force direction. In addition, stress concentration was observed in the overlapping area of the adjacent layers (red area in Figure 7b), where the stress value was significantly higher than that in the other areas. However, the maximum stress was approximately 4.3 MPa, which was lower than the ultimate tensile stress of PDMS (approximately 17 MPa). Therefore, the 3D-printed porous PDMS has excellent tensile properties for the requirements in typical environments.

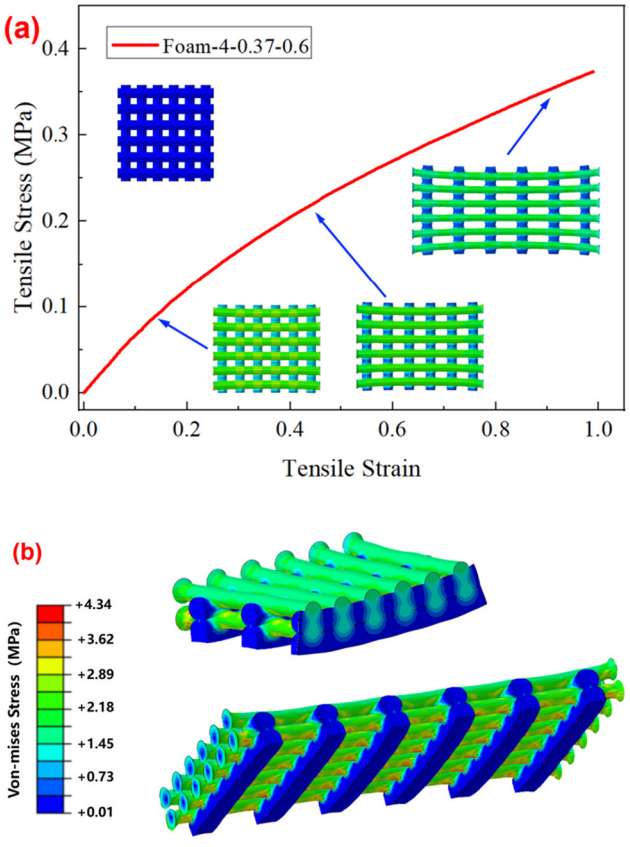

Figure 7: Tensile mechanical behaviors of porous PDMS model: (a) tensile stress–strain curve and (b) Von-Mises stress distributing graph of the model "Foam-4-0.37-0.6" at 100% tensile strain.

Figure 8 shows the effect of filament spacing on the tensile performance of the porous PDMS with filament diameters of 0.37, 0.31, and 0.25 mm. The resistance to

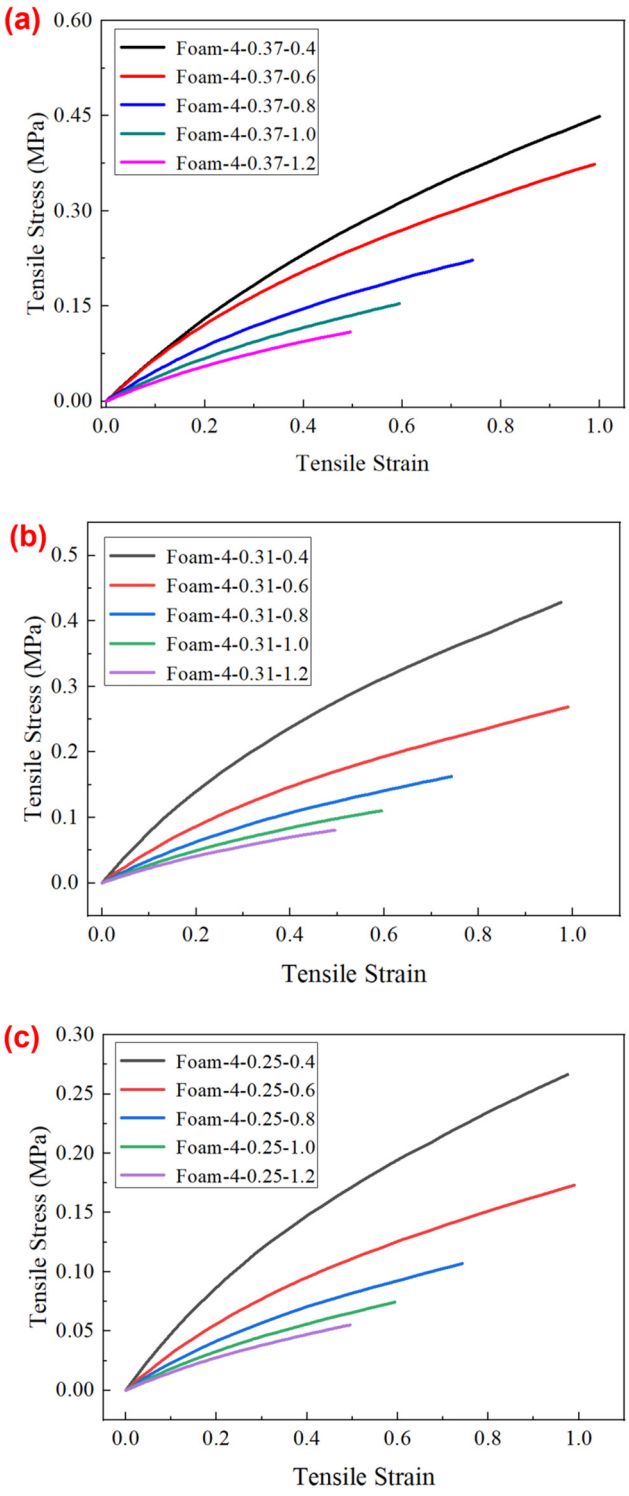

Figure 8: Effect of filament spacing on the tension behaviors of 3D-printed porous PDMS films with different filament diameters: (a) 0.37 mm, (b) 0.31 mm, and (c) 0.25 mm.

tensile deformation gradually increased as the filament spacing (l) decreased, provided that the diameter of the filament (d) was fixed. With the increase in filament diameter, the resistance to tensile deformation was enhanced when the filament spacing was fixed. Similar to the effects of increasing filament diameter or decreasing filament spacing on improving the resistance to compressive deformation, the adjustment of the printing parameters essentially affects the porosity of the porous PDMS, which, in turn, affects its tensile mechanical properties.

Therefore, consistent with the previous modulation of the compressive mechanical behavior of 3D-printed PDMS by controlling the porosity characteristic parameters, a similar approach was used to modulate the tensile mechanical behavior. By adjusting the filament spacing and diameter, the tensile behavior of the 3D-printed porous PDMS can be regulated, as shown in Figure 9a. In all FEMs, the tensile modulus E^* of the porous PDMS films reached a minimum of 0.13 MPa and a maximum of 0.85 MPa. To analyze this modulation mechanism quantitatively, the aforementioned data were fitted based on equation (3). As shown in Figure 9b, the predicted curves are also in good agreement with the simulated data, confirming that the FEMs can also provide theoretical guidance for the design of 3D-printed PDMS with superhydrophobic properties in terms of tensile mechanical behavior. It is important to point out that although samples are evaluated with only four layers in this study, the increase in the number of printed layers does not change the deformation mechanism of 3D-printed porous PDMS film under compressive and tensile loads in small deformation states, and therefore, the quantitative correlation between elastic modulus and structural features applies to 3D-printed films with more than four layers. However, when under large deformations, especially in compression, an increase in the number of printed layers may cause the structure to be more easily buckled, leading to the collapse of the microstructure.

4 Conclusions

This study presents a numerical simulation of the structure–mechanical relationship of 3D-printed porous PDMS films with superhydrophobic properties. The porous films exhibited a columnar force transfer path along the overlapping area of the adjacent filaments, which directly contributed to the compressive elastic modulus of the porous PDMS. Meanwhile, the 3D-printed porous PDMS possessed typical orthogonal anisotropy characteristics. The tensile stress in the PDMS filament along the force direction was significantly higher than that perpendicular to the force direction, and the tensile modulus was mainly attributed to the filament parallel to the force direction. In addition, the uniaxial compression and tensile properties could be controlled by adjusting the filament spacing and diameter. Therefore, a quantitative relationship was established between the relative density of porous PDMS and the relative elastic modulus (tensile and compressive). This study provides theoretical guidance for the structural–-functional integration design of 3D-printed superhydrophobic porous PDMS.

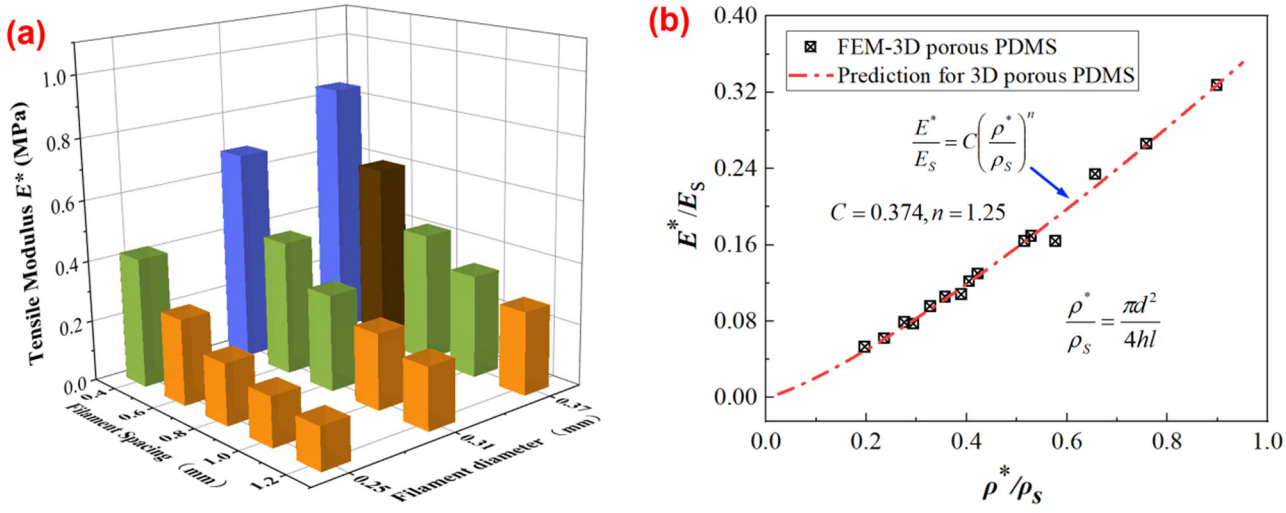

Figure 9: (a) Effects of the filament diameter and filament spacing on the tensile elastic modulus E^*. The histograms within the same color represent similar tensile elastic modulus E^*, and (b) relationship between the relative tensile modulus and the relative density of 3D-printed porous PDMS.

Funding information: The authors would like to acknowledge the financial support from the National Natural Science Foundation of China (No. 51873240), the Henan Provincial Science and Technology Research Project (No. 222102230080), the Henan Provincial Natural Science Foundation Youth Project (No. 232300420313), the Henan Key Laboratory of Grain and Oil Storage Facility and Safety Research Project (No.2023KF09), the Sichuan Science and Technology Program (No. 2022YFS0634), and the Key Research and Development Programs of Luzhou (No. 2022-GYF-12), the Talent Introduction Program of The Affiliated Stomatological Hospital of Southwest Medical University (No. 2022BS02), and the Innovative Leading Talents Program of The Affiliated Stomatological Hospital of Southwest Medical University (No. 2022LJ02).

Author contributions: Xiaowei Zhu, Zhoukun He, and Xiaorong Lan conceived and designed this study; Xiaowei Zhu, Yue Li, and Zhoukun He prepared the samples and wrote this manuscript; Yilun Shi, Lanjie Hou, Guoxian Wang, and Xiaorong Lan made the finite element analysis and revised this manuscript. All authors have accepted responsibility for the entire content of this manuscript and approved its submission.

Conflict of interest: The authors state no conflict of interest.

References

[1] He Z, Mu L, Wang N, Su J, Wang Z, Luo M, et al. Design, fabrication, and applications of bioinspired slippery surfaces. Adv Colloid Interface Sci. 2023;318:102948.
[2] He Z, Chen Y, Yang J, Tang C, Lv J, Liu Y, et al. Fabrication of Polydimethylsiloxane films with special surface wettability by 3D printing. Compos Part B: Eng. 2017;129:58–65.
[3] He Z, Ma M, Lan X, Chen F, Wang K, Deng H, et al. Fabrication of a transparent superamphiphobic coating with improved stability. Soft Matter. 2011;7:6435–43.
[4] Wu Y, Zhou S, You B, Wu L. Bioinspired design of three-dimensional ordered tribrachia-post arrays with re-entrant geometry for omniphobic and slippery surfaces. ACS Nano. 2017;11:8265–72.
[5] Chen K, Zhou S, Wu L. Self-healing underwater superoleophobic and antibiofouling coatings based on the assembly of hierarchical microgel spheres. ACS Nano. 2016;10:1386–94.
[6] Xiong Z, Yu H, Gong X. Designing photothermal superhydrophobic PET fabrics via in situ polymerization and 1,4-conjugation addition reaction. Langmuir. 2022;38:8708–18.
[7] Han X, Gong X. In situ, one-pot method to prepare robust superamphiphobic cotton fabrics for high buoyancy and good antifouling. ACS Appl Mater Interfaces. 2021;13:31298–309.
[8] Li L, Xu Z, Sun W, Chen J, Dai C, Yan B, et al. Bio-inspired membrane with adaptable wettability for smart oil/water separation. J Membr Sci. 2020;598:117661.
[9] Selim MS, Fatthallah NA, Higazy SA, Hao Z, Jing Mo P. A comparative study between two novel silicone/graphene-based nanostructured surfaces for maritime antifouling. J Colloid Interface Sci. 2022;606:367–83.
[10] Han K, Heng L, Zhang Y, Liu Y, Jiang L. Slippery surface based on photoelectric responsive nanoporous composites with optimal wettability region for droplets' multifunctional manipulation. Adv Sci. 2019;6:1801231.
[11] Martin S, Brown PS, Bhushan B. Fabrication techniques for bioinspired, mechanically-durable, superliquiphobic surfaces for water, oil, and surfactant repellency. Adv Colloid Interface Sci. 2017;241:1–23.
[12] Saji VS. Carbon nanostructure-based superhydrophobic surfaces and coatings. Nanotechnol Rev. 2021;10:518–71.
[13] He Z, Wang N, Mu L, Wang Z, Su J, Chen Y, et al. Porous polydimethylsiloxane films with specific surface wettability but distinct regular physical structures fabricated by 3D printing. Front Bioeng Biotechnol. 2023;11:1272565.
[14] Lyu J, Wu B, Wu N, Peng C, Yang J, Meng Y, et al. Green preparation of transparent superhydrophobic coatings with persistent dynamic impact resistance for outdoor applications. Chem Eng J. 2021;404:126456.
[15] Selim MS, Elmarakbi A, Azzam AM, Shenashen MA, El-Saeed AM, El-Safty SA. Eco-friendly design of superhydrophobic nano-magnetite/silicone composites for marine foul-release paints. Prog Org Coat. 2018;116:21–34.
[16] He Z, Wang N, Yang X, Mu L, Wang Z, Su J, et al. Antifouling induced by surface wettability of poly(dimethyl siloxane) and its nanocomposites. Nanotechnol Rev. 2023;12:20220552.
[17] He Z, Yang X, Mu L, Wang N, Lan X. A versatile "3M" methodology to obtain superhydrophobic PDMS-based materials for antifouling applications. Front Bioeng Biotechnol. 2022;10:998852.
[18] He Z, Yang X, Wang N, Mu L, Pan J, Lan X, et al. Anti-biofouling polymers with special surface wettability for biomedical applications. Front Bioeng Biotechnol. 2021;9:807357.
[19] He Z, Lan X, Hu Q, Li H, Li L, Mao J. Antifouling strategies based on super-phobic polymer materials. Prog Org Coat. 2021;157:106285.
[20] Selim MS, El-Safty SA, Shenashen MA, Higazy SA, Elmarakbi A. Progress in biomimetic leverages for marine antifouling using nanocomposite coatings. J Mater Chem B. 2020;8:3701–32.
[21] Selim MS, Azzam AM, Higazy SA, El-Safty SA, Shenashen MA. Novel graphene-based ternary nanocomposite coatings as ecofriendly antifouling brush surfaces. Prog Org Coat. 2022;167:106803.
[22] Guo T, Che P, Heng L, Fan L, Jiang L. Anisotropic slippery surfaces: Electric-driven smart control of a drop's slide. Adv Mater. 2016;28:6999–7007.
[23] Zhang Y, Jiao Y, Chen C, Zhu S, Li C, Li J, et al. Reversible tuning between isotropic and anisotropic sliding by one-direction mechanical stretching on microgrooved slippery surfaces. Langmuir. 2019;35:10625–30.
[24] Feng R, Song F, Xu C, Wang X-L, Wang Y-Z. A quadruple-biomimetic surface for spontaneous and efficient fog harvesting. Chem Eng J. 2021;422:130119.
[25] Wang X, Wang Z, Heng L, Jiang L. Stable omniphobic anisotropic covalently grafted slippery surfaces for directional transportation of drops and bubbles. Adv Funct Mater. 2020;30:1902686.
[26] Guo P, Wang Z, Han X, Heng L. Nepenthes pitcher inspired isotropic/anisotropic polymer solid–liquid composite interface: preparation, function, and application. Mater Chem Front. 2021;5:1716–42.

[27] Wu Y, Zeng J, Si Y, Chen M, Wu L. Large-area preparation of robust and transparent superomniphobic polymer films. ACS Nano. 2018;12:10338–46.
[28] Xiong Z, Huang J, Wu Y, Gong X. Robust multifunctional fluorine-free superhydrophobic fabrics for high-efficiency oil–water separation with ultrahigh flux. Nanoscale. 2022;14:5840–50.
[29] Li L, Bai Y, Li L, Wang S, Zhang T. A superhydrophobic smart coating for flexible and wearable sensing electronics. Adv Mater. 2017;29:1702517.
[30] Jia L-C, Nie R-P, Xu L, Yan D-X, Lei J, Li Z-M. Carbonized cotton textile with hierarchical structure for superhydrophobicity and efficient electromagnetic interference shielding. Compos Part A: Appl Sci Manuf. 2021;149:106555.
[31] Zhu Y, Chen M, Wu L. Synthesis of UV-responsive dual-functional microspheres for highly efficient self-healing coatings. Chem Eng J. 2021;422:130034.
[32] Bixler GD, Theiss A, Bhushan B, Lee SC. Anti-fouling properties of microstructured surfaces bio-inspired by rice leaves and butterfly wings. J Colloid Interface Sci. 2014;419:114–33.
[33] Yu C, Zhang L, Ru Y, Li N, Li C, Gao C, et al. Drop cargo transfer via unidirectional lubricant spreading on peristome-mimetic surface. ACS Nano. 2018;12:11307–15.
[34] Feng L, Li S, Li Y, Li H, Zhang L, Zhai J, et al. Super-hydrophobic surfaces: From natural to artificial. Adv Mater. 2002;14:1857–60.
[35] Selim MS, Yang H, Wang FQ, Fatthallah NA, Huang Y, Kuga S. Silicone/ZnO nanorod composite coating as a marine antifouling surface. Appl Surf Sci. 2019;466:40–50.
[36] Gong L, Zhang J, Wang W, Xiang L, Pan M, Yang W, et al. Ion-specific effect on self-cleaning performances of polyelectrolyte-functionalized membranes and the underlying nanomechanical mechanism. J Membr Sci. 2021;634:119408.
[37] Rasitha TP, Vanithakumari SC, Nanda Gopala Krishna D, George RP, Srinivasan R, Philip J. Facile fabrication of robust superhydrophobic aluminum surfaces with enhanced corrosion protection and anti-fouling properties. Prog Org Coat. 2022;162:106560.
[38] Chang J, He X, Yang Z, Bai X, Yuan C. Effects of chemical composition on the hydrophobicity and antifouling performance of epoxy-based self-stratifying nanocomposite coatings. Prog Org Coat. 2022;167:106827.
[39] Cao X, Pan J, Cai G, Xiao S, Ma X, Zhang X, et al. A chemically robust and self-healing superhydrophobic polybenzoxazine coating without fluorocarbon resin modification: Fabrication and failure mechanism. Prog Org Coat. 2022;163:106630.
[40] Li H, Cheng B, Gao W, Feng C, Huang C, Liu Y, et al. Recent research progress and advanced applications of silica/polymer nanocomposites. Nanotechnol Rev. 2022;11:2928–64.
[41] Zhang H, Tan J, Liu Y, Hou C, Ma Y, Gu J, et al. Design and fabrication of robust, rapid self-healable, superamphiphobic coatings by a liquid-repellent “glue + particles” approach. Mater Des. 2017;135:16–25.
[42] Zhang F, Qian H, Wang L, Wang Z, Du C, Li X, et al. Superhydrophobic carbon nanotubes/epoxy nanocomposite coating by facile one-step spraying. Surf Coat Technol. 2018;341:15–23.
[43] Qian H, Liu B, Wu D, Zhang F, Wang X, Jin L, et al. Magnetically responsive lubricant-infused porous surfaces with controllable lubricity and durable anti-icing performance. Surf Coat Technol. 2021;406:126742.
[44] Wang Y, Gao C, Zhao W, Zheng G, Ji Y, Dai K, et al. Large-area fabrication and applications of patterned surface with anisotropic superhydrophobicity. Appl Surf Sci. 2020;529:147027.
[45] Cheng L, Xu Q, Jia X, Zhang R, Bai S, Qin Y, et al. Anisotropic wetting properties of oblique nanowires array and their applications on water transportation and fog collection. Surf Interfaces. 2021;22:100784.
[46] Su Y, Zhao Y, Jiang S, Hou X, Hong M. Anisotropic Superhydrophobic Properties of Bioinspired Surfaces by Laser Ablation of Metal Substrate inside Water. Adv Mater Interfaces. 2021;8:2100555.
[47] Hans M, Müller F, Grandthyll S, Hüfner S, Mücklich F. Anisotropic wetting of copper alloys induced by one-step laser micro-patterning. Appl Surf Sci. 2012;263:416–22.
[48] Dong Z, Vuckovac M, Cui W, Zhou Q, Ras RHA, Levkin PA. 3D printing of superhydrophobic objects with bulk nanostructure. Adv Mater. 2021;33:2106068.
[49] Zhu X, Chen Y, Liu Y, Deng Y, Tang C, Gao W, et al. Additive manufacturing of elastomeric foam with cell unit design for broadening compressive stress plateau. Rapid Prototyp J. 2018;24:1579–85.
[50] Zhu X, Chen Y, Liu Y, Tang C, Liu T, Mei J, et al. Revisiting effects of microarchitecture on mechanics of elastomeric cellular materials. Appl Phys A. 2019;125:247.
[51] Somireddy M, Czekanski A. Anisotropic material behavior of 3D printed composite structures – Material extrusion additive manufacturing. Mater Des. 2020;195:108953.
[52] Marovič N, Ban I, Maver U, Maver T. Magnetic nanoparticles in 3D-printed scaffolds for biomedical applications. Nanotechnol Rev. 2023;12:20220570.
[53] Changyou Y, Jiang P, Jia X, Wang X. 3D printing of bioinspired textured surfaces with superamphiphobicity. Nanoscale. 2020;12:2924–38.
[54] Han Y, Lei H, Kaken H, Zhao W, Wang W, Wumanerjiang A, et al. 3D printing customized design of human bone tissue implant and its application. Nanotechnol Rev. 2022;11:1792–801.
[55] Wu Z, Shi C, Chen A, Li Y, Chen S, Sun D, et al. Large-scale, abrasion-resistant, and solvent-free superhydrophobic objects fabricated by a selective laser sintering 3D printing strategy. Adv Sci. 2023;10:2207183.
[56] Zhang X, Wang Q, Zou R, Song B, Yan C, Shi Y, et al. 3D-printed superhydrophobic and magnetic device that can self-powered sense a tiny droplet impact. Engineering. 2022;15:196–205.
[57] Barraza B, Olate-Moya F, Montecinos G, Ortega JH, Rosenkranz A, Tamburrino A, et al. Superhydrophobic SLA 3D printed materials modified with nanoparticles biomimicking the hierarchical structure of a rice leaf. Sci Technol Adv Mater. 2022;23:300–21.
[58] Wang P, Li C, Zhang D. Recent advances in chemical durability and mechanical stability of superhydrophobic materials: Multi-strategy design and strengthening. J Mater Sci Technol. 2022;129:40–69.
[59] Woo R, Chen G, Zhao J, Bae J. Structure–mechanical property relationships of 3D-printed porous polydimethylsiloxane. ACS Appl Polym Mater. 2021;3:3496–503.
[60] Zhu X, Shi Y, Sun F, Hou F, Li Y, Wen J, et al. Stress relaxation behavior of 3D printed silicone rubber foams with different topologies under uniaxial compressive load. Compos Commun. 2023;38:101475.
[61] Moroni L, de Wijn JR, van Blitterswijk CA. 3D fiber-deposited scaffolds for tissue engineering: Influence of pores geometry and architecture on dynamic mechanical properties. Biomaterials. 2006;27:974–85.
[62] Treloar L. The physics of rubber elasticity. Oxford: Oxford University Press; 1975.
[63] Gibson LJ, Ashby MF. Cellular Solids: Structure and Properties. Cambridge: Cambridge University Press; 2003.